International Journal of Heat and Mass Transfer 103 (2016) 1313–1326

Contents lists available at ScienceDirect

International Journal of Heat and Mass Transfer

journal homepage: www.elsevier.com/locate/ijhmt

# Thermal and thermodynamic performance, and pressure oscillations of refrigeration loop employing large micro-channel evaporators

Seunghyun Lee, Issam Mudawar *

*Boiling and Two-Phase Flow Laboratory (PU-BTPFL), School of Mechanical Engineering, Purdue University, 585 Purdue Mall, West Lafayette, IN 47907, USA*

ARTICLE INFO

*Article history:*
Received 20 May 2016
Received in revised form 7 August 2016
Accepted 11 August 2016
Available online 20 August 2016

*Keywords:*
Micro-channel
Flow boiling
Condensation
Instabilities
Exergy analysis
Refrigeration cycle

ABSTRACT

This study explores the implementation of two large micro-channel heat exchangers as evaporators in a refrigeration cycle intended for thermal management onboard future space vehicles. Examined are thermal performances of the two heat exchangers, thermodynamic performance of the refrigeration cycle, and system instabilities. Because of quality differences, different two-phase flow patterns and dryout effects are encountered in the two heat exchangers. A trade-off exists between optimum performances of the evaporators and compressor, with former favoring outlet quality values below unity to guard against dryout, and the compressor favoring a quality equal to or exceeding unity to preclude internal damage to the compressor from entrained droplets. Thermodynamic analysis of the refrigeration cycle shows exergy destruction is minimum when the avionics HX's outlet quality is close to unity. The system is shown to be susceptible to instability resulting from interactions between compressible volumes both upstream and downstream of the condenser, and inertia of liquid in the condenser. This instability is manifest by pressure oscillations that are sensitive to both flow rate and evaporator heat input.



## 1. Introduction

### 1.1. Applications of mini/micro-channel cooling

Mini/micro-channel cooling has received unprecedented attention in recent years as a means to cope with the need to tackle increasing heat dissipation from smaller and more lightweight electronic and power packages. This includes such applications as computer data centers, avionics, hybrid vehicle power electronics, laser and microwave directed energy weapons, and X-ray medical devices [1,2]. While initial emphasis was placed on single-phase micro-channel heat sinks [3], crucial disadvantages of these single-phase devices quickly became apparent when dissipating very high heat fluxes. Since single-phase heat sinks rely on the coolant's sensible heat rise to remove the heat, dissipation of high fluxes resulted in large stream-wise temperature gradients in both coolant and device. Later, two-phase mini/micro-channel cooling was recommended to greatly reduce temperature gradients by relying on the coolant's latent in addition to sensible heat, maintaining a fairly constant coolant saturation temperature [1,2]. These advantages were the impetus for numerous studies addressing various transport characteristics of two-phase micro-channel flow, including pressure drop and heat transfer coefficient, *e.g.* [4–11].

### 1.2. Use of two-phase mini/micro-channel heat sinks as evaporators in cooling systems

Two-phase mini/micro-channel heat sinks have also shown tremendous versatility of implementation into different loop configurations, such as conventional pumped loops and vapor compression loops [2], as well as pumpless gravity-driven loops [12]. They have also been combined with jet impingement into hybrid cooling schemes [13–15] and applications involving large fluctuations in body force [16].

Initial emphasis in the implementation of two-phase mini/micro-channel heat sinks was placed on high-flux CPU cooling. Bowers and Mudawar [17] used R113 to test the cooling performances of two 10 × 10-mm$^2$ heat sinks containing parallel circular channels extending between constant pressure inlet and outlet plenums. The first contained 17 of 0.51-mm micro-channels that were formed in a nickel plate that was soldered to a copper heat sink, while the other featured 3 of 2.54-mm mini-channels that were formed directly in a copper heat sink. While both heat sinks produced fairly similar thermal performances, achieving critical heat flux (CHF) values in excess of 200 W/cm$^2$, much higher pressure drop was encountered in the micro-channel heat sink following the commencement of nucleate boiling.

* Corresponding author.
*E-mail address:* mudawar@ecn.purdue.edu (I. Mudawar).
*URL:* https://engineering.purdue.edu/BTPFL (I. Mudawar).

http://dx.doi.org/10.1016/j.ijheatmasstransfer.2016.08.031
0017-9310/

**Nomenclature**

| | |
|---|---|
| $A$ | cross-sectional area |
| $a$ | Fourier series coefficient |
| $A_{base}$ | total base area of heat sink |
| $b$ | Fourier series coefficient |
| $COP$ | coefficient of performance |
| $Cv$ | valve flow coefficient |
| $D_h$ | hydraulic diameter |
| $f$ | Helmholtz resonance frequency |
| $G$ | mass velocity |
| $h$ | enthalpy |
| $H_{ch}$ | micro-channel height |
| $h_{fg}$ | latent heat of vaporization |
| $H_{tc}$ | distance between thermocouple and base of micro-channel |
| $h_{tp}$ | local two-phase heat transfer coefficient |
| $h_{tp,avg}$ | average heat transfer coefficient |
| $I$ | irreversibility |
| $k$ | thermal conductivity |
| $L$ | micro-channel length |
| $L_f$ | length of liquid section |
| $m$ | fin parameter |
| $\dot{m}$ | mass flow rate |
| $\dot{m}_*$ | mass flow rate through throttle valves in pressure oscillations model |
| $N$ | number of thermocouples in heat sink |
| $P$ | pressure |
| $Q$ | heat input |
| $q''$ | heat flux based on total base area of heat sink |
| $s$ | entropy |
| $S_{gen}$ | entropy generated |
| $T$ | temperature |
| $t$ | time |
| $T_0$ | ambient temperature |
| $V$ | volume |
| $W$ | work |
| $W_{ch}$ | micro-channel width |
| $W_w$ | half-width of copper sidewall separating micro-channels |
| $X_{destroyed}$ | exergy destroyed |
| $x_e$ | thermodynamic equilibrium quality |
| $z$ | coordinate along micro-channel |

*Greek symbols*

| | |
|---|---|
| $\eta$ | fin efficiency |
| $\gamma$ | throttle valve constant |
| $v$ | speed of sound in superheated vapor or two-phase flow |
| $\omega$ | angular frequency |
| $\tau$ | period |

*Subscripts*

| | |
|---|---|
| *avionics* | avionics HX |
| *b* | bottom of micro-channel |
| *crew* | crew HX |
| *d* | downstream compressible volume |
| *f* | liquid |
| *in* | micro-channel inlet |
| *out* | micro-channel outlet |
| *s* | solid (copper) |
| *sat* | saturation |
| *sink* | heat sink |
| *tc* | thermocouple |
| *tp* | two phase |
| *u* | upstream compressible volume |
| *w* | micro-channel wall |
| 0 | ambient condition; initial condition |

Lee and Mudawar [18–20] explored both the fundamental and practical issues associated with incorporating a micro-channel heat sink as evaporator in a compact refrigeration loop using R134a as coolant. Their $25.3 \times 25.3$-mm$^2$ copper heat sink contained 53 of 231-μm wide and 713-μm tall micro-channels. They were able to achieve heat fluxes up to 93.8 W/cm$^2$ without incurring CHF. More importantly, they demonstrated the effectiveness of incorporating a micro-channel heat sink as evaporator in the refrigeration cycle, addressing the trade-off between the need to maintain sufficient liquid at the evaporator's outlet to guard against CHF, and avoiding the potentially damaging excessive liquid inflow to the compressor.

### 1.3. Flow instabilities in two-phase systems

In two review articles addressing instabilities in two-phase systems, Boure et al. [21] and Kakaç and Bon [22] identified two major categories of dynamic flow instabilities, *pressure-drop oscillations* and *density-wave oscillations*. To determine the dominant instability, they compared steady-state pressure-drop versus mass flow rate curves representing the two-phase heat transfer region (internal characteristics curve) and the fluid supply system (external characteristics curve). The pressure-drop oscillations occurred in the two-phase flow region where the slope of the internal characteristics curve is negative and the slope of the external characteristics curve is more negative than the former. The density-wave oscillations occurred where the slope of the internal characteristics curve is positive in the low mass flow range, causing the density to change repetitively as the mass flow rate oscillated. Investigators employed both the HEM [23] and the Drift-flux Model [24] to determine pressure drop across the boiling section to explore both instabilities, especially for boiling in vertical upflow. Also employed to investigate the pressure-drop oscillations is the Lumped Parameter Model [25–29]. This model simplifies momentum effects by simulating the flow boiling section as a lumped pressure drop component, neglecting the detailed pressure drop behavior within. For the pressure-drop oscillations, the pressure drop characteristics are described by a third-order equation for flow rate, reducing momentum interactions to a Van der Pol equation.

More recently, rising interest in the use of two-phase mini/micro-channel heat sinks created a need to investigate two-phase flow instabilities specific to flow boiling in small diameter channels. Qu and Mudawar [30,31] experimentally identified two types of flow instabilities in mini/micro-channel heat sinks: severe pressure-drop oscillations and mild parallel-channel oscillations. The severe oscillations occurred in the absence of a flow resistance upstream of the heat sink as a result of dynamic interactions between vapor generation in the heat sink and upstream compressible volume in the flow loop. This type of instability was manifest by the boundary between the single-phase liquid and two-phase mixture in all heat sink channels fluctuating in unison between the inlet and outlet. By installing a throttling valve upstream of the heat sink, the severe pressure-drop oscillation was virtually eliminated due to suppression of the dynamic interactions with the upstream compressible volume. With adequate upstream throttling, only the second mild parallel-channel instability was encountered. This instability took the form of random

fluctuations of boiling boundary between micro-channels, and was attributed to density-wave oscillations within each channel and feedback interaction between channels.

Another type of instability in two-phase systems is the *chugging effect* [32] associated with flow condensation. This phenomenon was encountered in experiments consisting of a pipe carrying steam in downflow into a subcooled water pool, where the stream was converted to water by direct contact condensation. Chugging was manifest by periodic oscillations of the interface between the steam and water within the pipe. When the interface moved out of the tube, pressure in the tube's upstream header decreased rapidly and intense condensation ensued. The decreased header pressure now drew liquid back into the tube, which, in turn, caused the header pressure to rise again and push the interface out of the tube. The amplitude and frequency of oscillations associated with chugging were modeled by incorporating the inertia of the liquid column [33].

### 1.4. Objective of study

The present study is a follow-up to recent investigations by the authors concerning the development of a thermal control system (TCS) for future space vehicles. This system offers the versatility of operation in vapor compression mode, two-phase pumped mode, or single-phase pumped mode, as dictated by heat load requirements and external temperature for the specific phase of the space mission [34]. This study concerns TCS operation in the vapor compression mode, with refrigerant R134a used to extract heat from crew and avionics using two separate micro-channel evaporators. In [35], the authors addressed the steady state two-phase flow and heat transfer regimes encountered in the two evaporators. This was followed in [36] by assessment of flow oscillations in the evaporators.

The present study addresses the following practical concerns associated with incorporating large area micro-channel evaporators into a refrigeration cycle:

1. Cooling performance of evaporators, including axial variations of heat sink temperature and heat transfer coefficient for wet and dry compression conditions.
2. Assessment of refrigeration cycle performance using first and second laws of thermodynamics.
3. Experimental and analytical investigation of dynamic flow oscillations in the condenser.

## 2. Experimental methods

### 2.1. Refrigeration loop

Fig. 1(a) shows a schematic diagram of the refrigeration loop assembled for the present study. R134a is selected as optimum working fluid based on thermodynamic performance, maximum system pressure and flow rate requirements, and both safety and environmental considerations [34]. The key components of the refrigeration loop are the crew HX and avionics HX, which are sized to simulate, respectively, metabolic heat input from the crew and heat generation from the avionics in a spacecraft thermal control system (TCS). The heat input increases R134a quality along the

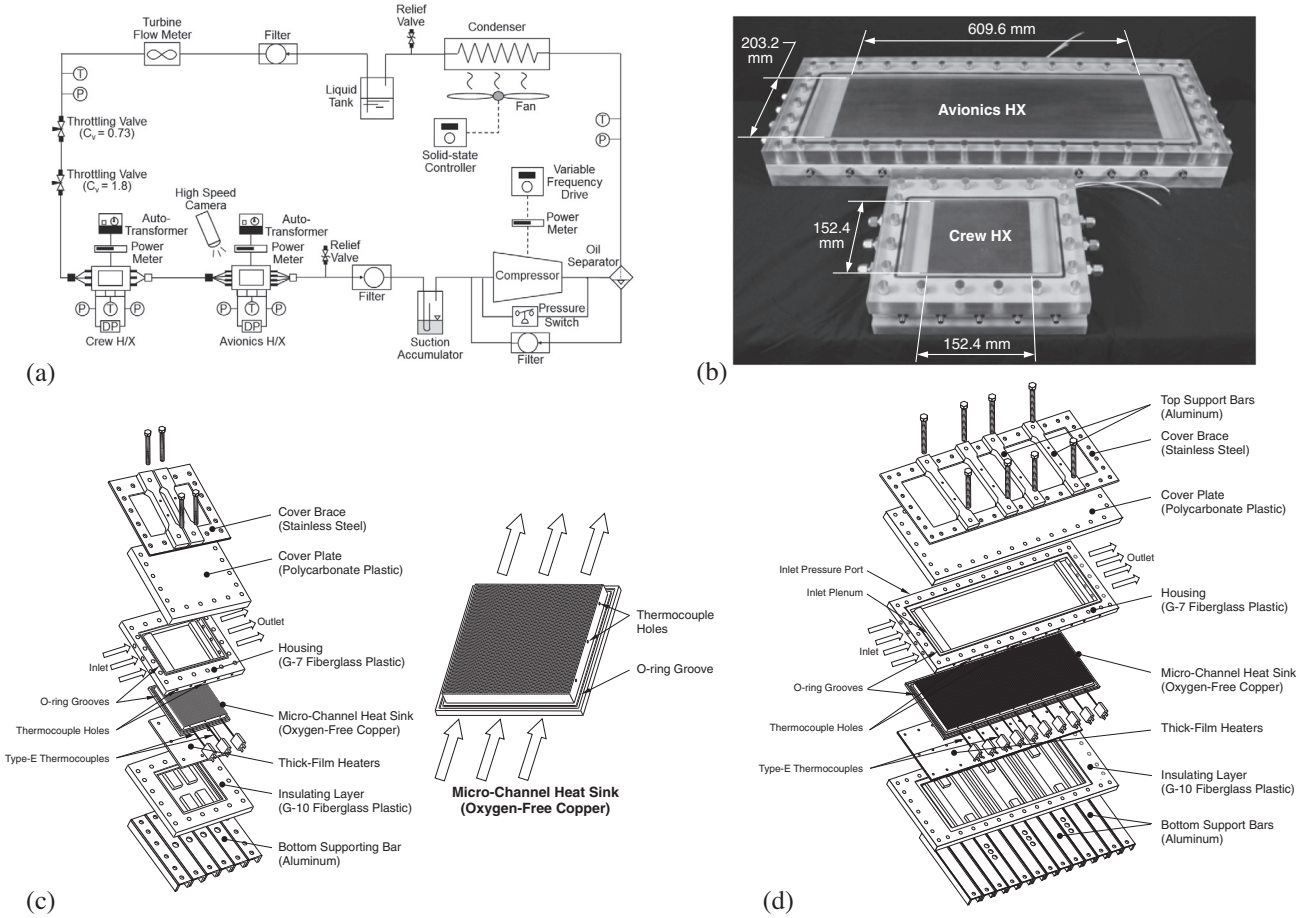


**Fig. 1.** (a) Schematic diagram of vapor compression loop. (b) Photo of avionics HX and crew HX. (c) Exploded view of crew HX. (d) Exploded view of avionics HX.

micro-channels in both heat exchangers. Because of the relative locations of the two heat exchangers, the R134a enters the upstream crew HX as a two-phase mixture, and encounters gradual changes in flow pattern from bubbly/slug to annular (with partial annular film dry-out or mist flow occurring under high heating conditions), and the quality increases to highest level at the outlet of the avionics HX. The R134a vapor temperature and pressure are increased by the compression process, following which the vapor is passed through an air-cooled condenser where it is returned to subcooled liquid state. The throttling valves decrease liquid pressure by isenthalpic expansion, causing the liquid to flash into a saturated two-phase mixture at the crew HX's inlet. Additional details concerning the vapor compression loop and its components and instrumentation are available in [35].

The condenser plays a key role in the instabilities discussed in this study. Unlike the evaporators in the present facility, which employ small flow passages, the condenser uses conventional macro passages. This air-cooled condenser features a wavy fin-and-tube construction, with the refrigerant flow divided into three parallel serpentine horizontal tubes that merged into a single line

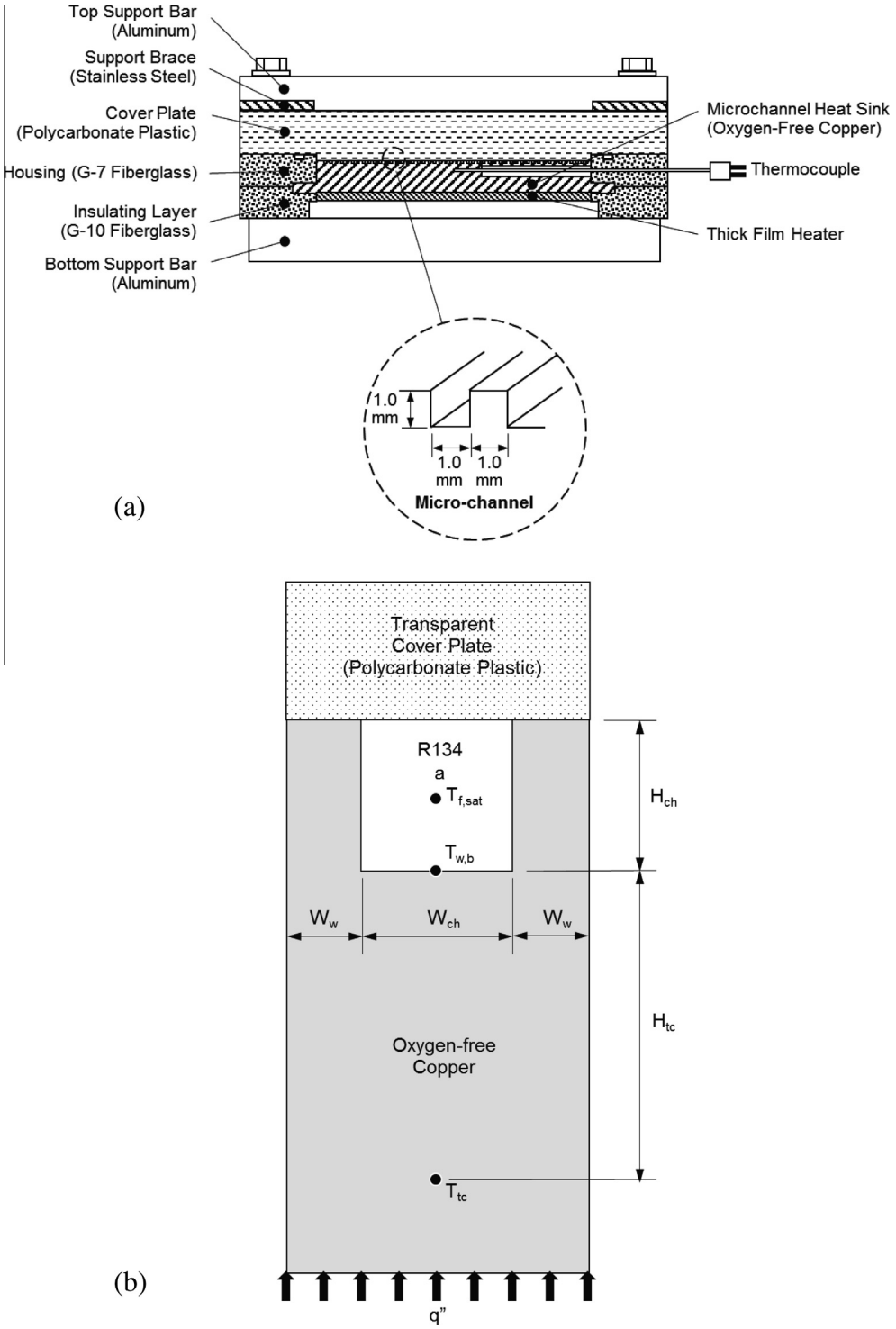


**Fig. 2.** (a) Cross-sectional view of avionics HX. (b) Micro-channel heat sink unit cell in both crew HX and avionics HX.

at the exit. The tube's inner diameter is 9.525 mm and total length of each of the three tubes is 13.34 m.

### 2.2. Construction of crew HX and avionics HX

Fig. 1(b) shows photos of the crew HX and avionics HX, with respective exploded views provided in Fig. 1(c) and (d). The micro-channels in each heat exchanger are machined into the top surface of a heat sink made from oxygen-free copper. Uniform heat flux is supplied from a Watlow thick-film heater embedded beneath the heat sink. The copper heat sink temperatures are measured at several axial locations using type-E thermocouples. The heat sink and thick film heater in each heat exchanger are inserted in an insulating housing made from G-7 fiberglass and fitted with a bottom insulating layer made from G-10 fiberglass. A top transparent cover plate made from polycarbonate plastic (Lexan) forms top walls for the micro-channels. The cover plate also provides video access to the two-phase flow inside the micro-channels. The video system consists of a Photron Ultima APX high speed camera fitted with a 105-mm Nikkor lens. A top metal brace and bottom support bars press the multiple layers of heat exchanger together as illustrated in Fig. 2(a), and serve to prevent distortion or buckling of intermediate layers.

Table 1 provides detailed information concerning the heat sink in each heat exchanger, including length, width, number of parallel micro-channels, axial locations of heat sink thermocouples, and ranges of heat flux and mass velocity. The heat sink in the crew HX is 152.4-mm long, 152.4-mm wide, and contains 75 parallel $1 \times 1\ mm^2$ micro-channels. The heat sink in the larger avionics HX is 609.6-mm long, 203.2-mm wide, and contains 100 parallel micro-channels having the same $1 \times 1\ mm^2$ cross-section. Larger size of the avionics HX is intended to tackle the much greater avionics heat generation compared to the crew's metabolic heat load.

### 2.3. Determination of thermodynamic equilibrium quality

Subcooled liquid exiting the condenser is converted to a two-phase mixture as it passes through the throttling valves, which decrease pressure to the desired crew HX's inlet pressure. Assuming isenthalpic pressure drop across the valves, the fluid's enthalpy at the inlet to the crew HX, $h_{crew,in}$, is equal to the enthalpy determined from pressure and temperature measurements of liquid upstream of the throttling valves. The crew HX's inlet quality, $x_{e,crew,in}$, is determined from the relation

$$x_{e,crew,in} = (h_{crew,in} - h_f)/h_{fg}, \tag{1}$$

where $h_f$ and $h_{fg}$ are determined from the saturated pressure measured at the crew HX's inlet. The crew HX's outlet quality is determined by applying energy balance to the crew HX,

$$x_{e,crew,out} = x_{e,crew,in} + (q''_{crew} A_{base})/\dot{m} h_{fg}, \tag{2}$$

where $q''_{crew}$ is the heat flux based on the heat sink's bottom area, $A_{base}$, and $\dot{m}$ the total flow rate of R134a.

### 2.4. Determination of Heat Transfer Coefficient

Fig. 2(b) shows a representative micro-channel unit cell comprised of a single micro-channel, two copper half sidewalls, copper bottom wall, and top polycarbonate plastic cover. Detailed dimensions of the cell are provided in Table 2. A uniform heat flux from the unit cell's underside is conducted upwards through the copper and transferred to the fluid passing through the micro-channel. Assuming the sidewalls serve as fins with efficiency $\eta$, the micro-channel's heat transfer coefficient, $h_{tp}$, can be determined by applying energy balance to the unit cell, which yields

$$h_{tp} = \frac{q''(W_{ch} + 2W_w)}{(T_{w,b} - T_{f,sat})(W_{ch} + 2\eta H_{ch})}. \tag{3}$$

The channel bottom wall temperature, $T_{w,b}$, in Eq. (3) is determined from the thermocouple temperature, $T_{tc}$, by assuming one-dimensional heat conduction between the planes of the thermocouple and micro-channel's bottom wall.

**Table 2**
Dimensions of micro-channel heat sink unit cell in both crew HX and avionics HX.

| $W_w$ [mm] | $W_{ch}$ [mm] | $H_{ch}$ [mm] | $H_{tc}$ [mm] |
|---|---|---|---|
| 0.5 | 1.0 | 1.0 | 4.08 |

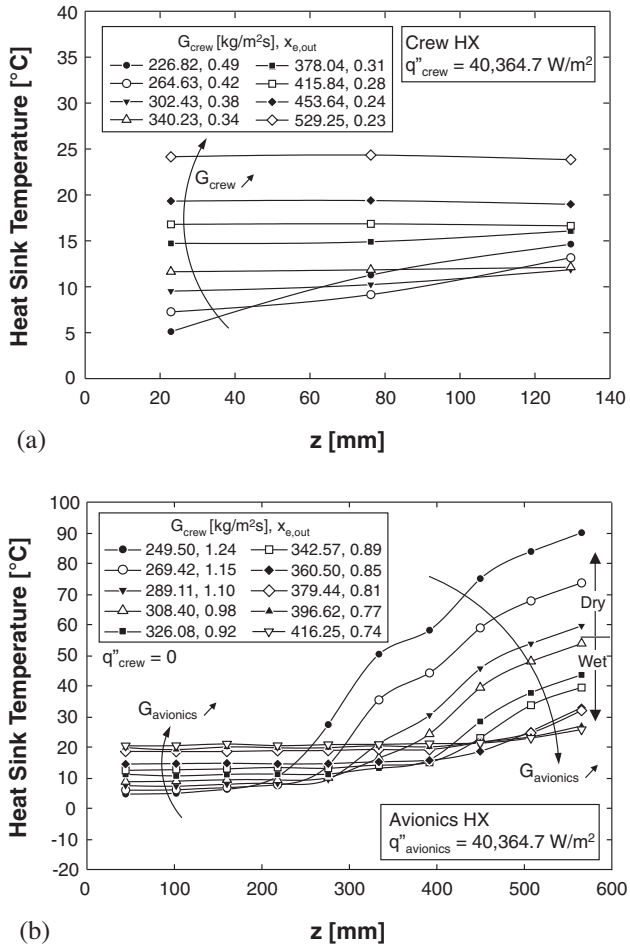


**Fig. 3.** Axial variations of heat sink temperature for different mass velocities and exit qualities in (a) crew HX and (b) avionics HX.

**Table 1**
Crew HX and avionics HX micro-channel heat sink dimensions.

| | Length [mm] | Width [mm] | Number of Channels | Thermocouple axial locations [mm] | Heat flux [W/m²] | Mass velocity [kg/m²s] |
|---|---|---|---|---|---|---|
| Crew HX | 152.4 | 152.4 | 75 | 22.9, 76.2, 129.5 | 8072.9–48,437.6 | 229.33–530.72 |
| Avionics HX | 609.6 | 203.2 | 100 | 44.2, 102.1, 160.0, 217.9, 275.8, 333.8, 391.7, 434.3, 507.5, 565.4 | 8072.9–44,401.1 | 152.9–434.31 |

$$T_{w,b} = T_{tc} - (q''H_{tc})/k_s, \quad (4)$$

where $H_{tc}$ and $k_s$ are the distance between the thermocouple junction and micro-channel's bottom wall, and thermal conductivity of copper, respectively. The fin efficiency is given by $\eta = \tanh(mH_{ch})/(mH_{ch})$, where $m$ is the fin parameter given by $m = \sqrt{h_{tp}/(k_s W_w)}$ [37].

## 3. Experimental results

### 3.1. Heat transfer characteristics of micro-channel heat exchangers

As discussed in [35], two important phenomena were observed to compromise cooling effectiveness in micro-channel evaporators. The first, *intermittent dryout*, which is associated with relatively lower quality flows, $x_{e,out} < 0.35$, occurs in mostly slug flow and is manifest by localized vapor blanket formation within the liquid slugs or dryout within the liquid film surrounding the elongated vapor bubbles. The second, *dryout incipience*, is associated with relatively high qualities, $x_{e,out} > 0.5$, and occurs in annular flow when the annular film begins to dry out. As discussed below, these two phenomena have a strong bearing on axial variations of the heat transfer coefficient in the micro-channel heat exchangers.

Since R134a enters the crew HX as a saturated two-phase mixture, heat sink temperature in this heat exchanger is closely related to saturation temperature and mass flow rate. Fig. 3(a) shows thermocouple temperatures along the crew HX's heat sink are fairly constant along the flow direction for high mass velocities, but increase downstream for lower mass velocities. This trend is closely related to intermittent dryout associated with high heat fluxes and low mass velocities for the relatively low quality range of the crew HX as discussed in [35]. This type of dryout occurs downstream, causing a large reduction in the heat transfer coefficient and a large increase in heat sink temperature. For $q''_{crew}$ = 40,364.7 W/m$^2$ and $G_{crew}$ = 302.43 kg/m$^2$s, Fig. 3(a) shows the heat sink temperature begins to increase downstream where intermittent dryout is initiated around $z$ = 129.5 mm.

The avionics HX is both much longer than, and located downstream from the crew HX, rendering it susceptible to the more drastic dryout incipience compared to intermittent dryout in the crew HX. Due to high quality values, annular flow is more prevalent in the avionics HX, and incipient dryout results from dry wall patches, whose axial span and frequency increase along the heat sink, causing an appreciable increase in the sink temperature. Fig. 3(b) shows the thermocouple measurements of the avionics HX's heat sink temperature follow different trends relative to mass velocity upstream versus downstream. The heat sink temperatures for a given $G_{avionics}$ are fairly constant upstream, where quality is lowest, and increase downstream because of high qualities and greater likelihood for dryout incipience. Notice that the lowest $G_{avionics}$ value, where heat sink temperature is lowest upstream, culminates in the largest temperature rise and highest heat sink temperatures downstream. This trend is caused by greater susceptibility to downstream dryout incipience at low compared to high $G_{avionics}$ values. For $q''_{avionics}$ = 40,364.7 W/m$^2$ and $G_{avionics}$ = 379.44 kg/m$^2$s, Fig. 3(b) shows the beginning of a large downstream rise in the heat sink temperature with incipient dryout occurring around $z$ = 565.4 mm.

For very high exit quality values approaching or exceeding unity, the annular film is completely evaporated and the annular flow pattern replaced by mist flow. Here, droplet impact with the

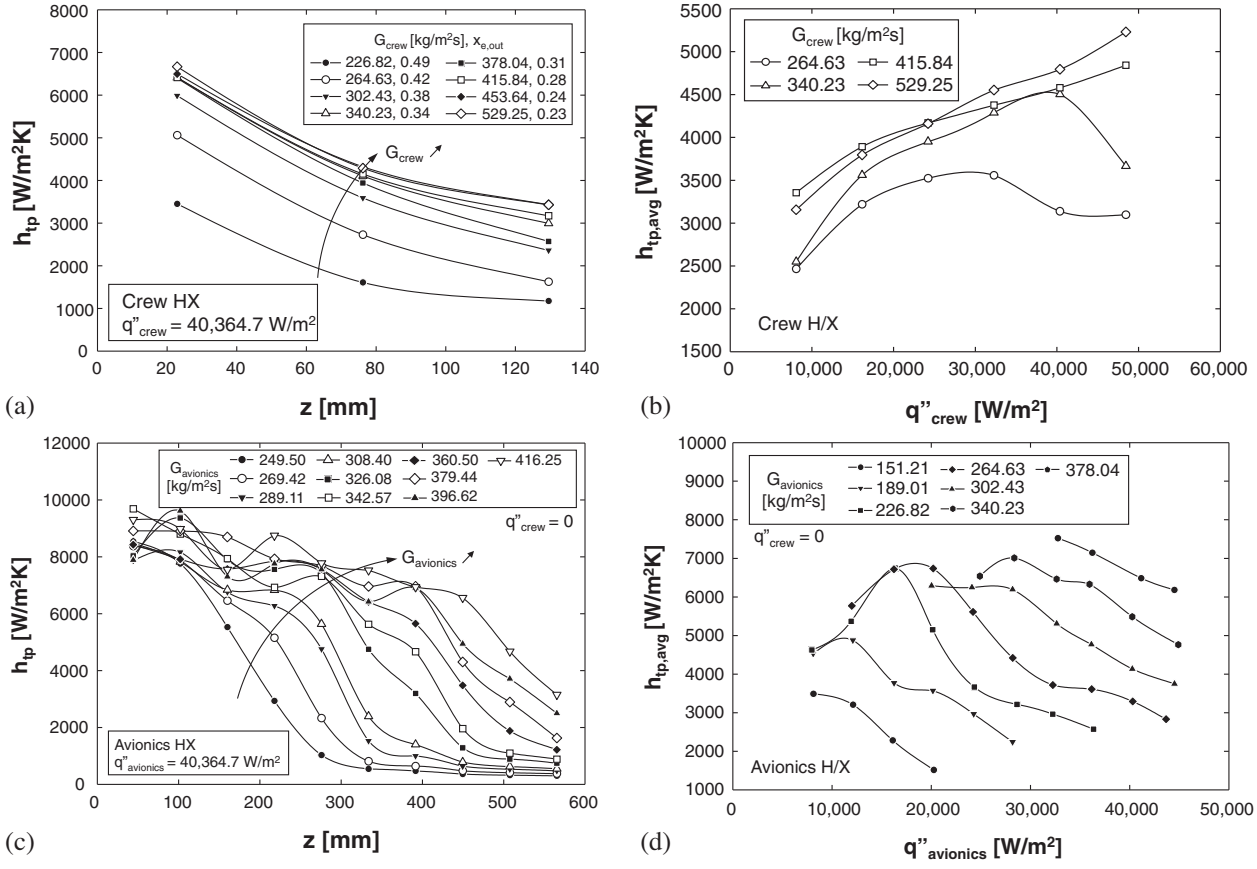


**Fig. 4.** (a) Variations of $h_{tp}$ along crew HX for different mass velocities. (b) Variations of crew HX's average $h_{tp}$ with heat flux for different mass velocities. (c) Variations of $h_{tp}$ along avionics HX for different mass velocities. (d) Variations of avionics HX's average $h_{tp}$ with heat flux for different mass velocities.

channel walls provides only minimal cooling, and the heat sink temperature increases drastically. This poses an important tradeoff between the need to maintain $x_{e,avionics,out} < 1$ (wet compression) to provide adequate cooling, and to achieve reliable compressor performance by maintaining $x_{e,avionics,out} > 1$ (dry compression). Fig. 3 (b) shows dry compression shifts dryout incipience upstream and wet compression downstream. Under wet compression conditions, the compressor in the present refrigeration loop is protected by a suction accumulator that employs a metering orifice to vaporize any liquid accrued on the bottom of the accumulator, allowing only vapor to be supplied to the compressor. Should the suction accumulator fail to fully vaporize the liquid, the scroll compressor protects itself by vaporizing liquid droplets with its rotor heat before the refrigerant enter the scroll, where the compression takes place.

The trends of heat sink temperature are also reflected in those of the heat transfer coefficient for both the crew HX and avionics HX. Fig. 4(a) shows $h_{tp}$ for the crew HX decreases along the flow direction and increases with increasing mass velocity. The axial decrease is the combined outcome of axial variations in both flow pattern and saturation temperature. Pressure drop along the crew HX decreases the saturation temperature. Combined with the relatively weak axial variations of heat sink temperature, this causes $h_{tp}$ to decrease monotonically along the channels.

Defined according to

$$\bar{h}_{tp} = \frac{1}{L}\int_0^L h_{tp}(z)dz, \tag{5}$$

the average heat transfer coefficient for the crew HX is shown to increase initially with increasing $q''_{crew}$, Fig. 4(b), as nucleation is intensified within predominantly bubbly/slug flow. However, the trends at high heat fluxes are different for low versus high $G_{crew}$. While $h_{tp,avg}$ continues to increase with increasing $q''_{crew}$ at high $G_{crew}$, the opposite trend is observed for low $G_{crew}$ as intermittent dryout triggers increased wall exposure to vapor.

Fig. 4(c) shows the downstream decrease in $h_{tp}$ along the avionics HX is encountered for the entire range of $G_{avionics}$. This trend is related to the prevalence of annular flow for this heat exchanger and commencement of dryout incipience downstream. Moreover, the lowest $G_{avionics}$ values are shown yielding vanishingly small values of $h_{tp}$ downstream, which is the outcome of the transition from annular to mist flow. And unlike the crew HX, Fig. 4(d) shows $h_{tp,avg}$ for the avionics HX decreases downstream for both low and high $G_{avionics}$. This trend is a reflection of the prevalence of downstream dryout incipience in the avionics HX.

### 3.2. Thermodynamic performance of refrigeration cycle

Fig. 5(a) shows temperature-entropy ($T$-$s$) diagram for the thermodynamic cycle for $q''_{avionics} = 24{,}218.8\ \mathrm{W/m^2}$ and $G_{avionics} = 170.11\ \mathrm{kg/m^2 s}$, with zero power input to the crew HX. Indicated in this figure are important transition points associated with the thermodynamic cycle. Points 1–2–3 correspond to heat absorption by the avionics HX, and the refrigerant changing phase from saturated two-phase mixture to saturated vapor (1–2), and afterwards to superheated vapor (2–3 for dry compression). Points 3–4 are associated with pressure rise of superheated vapor by the scroll compressor. Points 4–5–6–7 corresponds to heat removal by the condenser, first by changing refrigerant from superheated to saturated vapor (4–5), then from saturated vapor to saturated liquid (5–6), and eventually to subcooled liquid at higher pressure (6–7). Finally, points 7–1 indicate isenthalpic pressure drop across the throttling valves to saturated two-phase mixture at the evaporator inlet. In Fig. 5(a), refrigerant enthalpy, $h$, and entropy, $s$, at points 4 and 7 are determined from direct measurements of

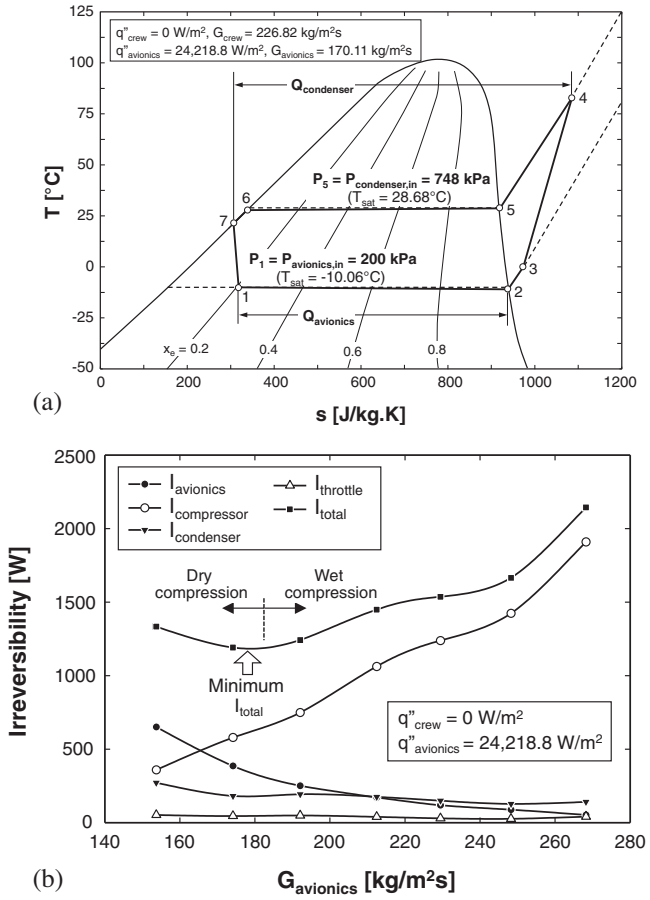


**Fig. 5.** (a) Temperature-entropy diagram for dry-compression with $q''_{crew} = 0$, $q''_{avionics} = 24{,}218.8\ \mathrm{W/m^2}$ and $G_{avionics} = 170.11\ \mathrm{kg/m^2 s}$. (b) Variations of irreversibilities of individual components and entire cycle with $G_{avionics}$ for $q''_{avionics} = 24{,}218.8\ \mathrm{W/m^2}$.

pressure and temperature. $h$ and $s$ at point 1 are calculated by assuming isenthalpic expansion across the throttling valves to the pressure measured at point 1, and at point 3 by using energy balance for the avionics HX, neglecting the minute adiabatic pressure drop across the crew HX. The $T$–$s$ diagram serves to assess cycle efficiency using the second law of thermodynamics.

Exergy analysis has been employed with refrigeration cycles [38–40], and design strategy to minimize entropy generation for different thermal components suggested [41]. Additionally, exergy destruction analysis has been conducted to assess the effects of wet compression for each component of the refrigeration cycle. Irreversibility, $I$, associated with the exergy destroyed, $X_{destroyed}$, is expressed in terms of entropy generation,

$$I = \dot{X}_{destroyed} = T_0 \dot{S}_{gen}, \tag{6}$$

where $T_0$ is the ambient temperature. Entropy generation for steady flow through a control volume with single input and single output is expressed as

$$\dot{S}_{gen} = \dot{m}(s_{out} - s_{in}) - \sum \frac{Q_k}{T_k}, \tag{7}$$

where $Q_k$ is the rate of heat input, which is positive when the heat is supplied to the control volume, and $T_k$ is the wall temperature where the heat transfer occurs. The rate of exergy destroyed in the avionics HX is the net effect of exergy destruction due to entropy change across the heat exchanger and heat supplied to the fluid,

$$I_{avionics} = T_0\left[\dot{m}(s_3 - s_1) - \frac{Q_{avionics}}{T_{sink}}\right] = T_0\dot{m}\left[(s_3 - s_1) - \frac{(h_3 - h_1)}{T_{sink}}\right], \quad (8)$$

where $T_{sink}$ is the average of the avionics HX's ten heat sink thermocouple temperatures,

$$T_{sink} = \frac{1}{N}\sum_{i=1}^{N} T_i, \quad (9)$$

and $N = 10$. With no heat input during the compression process, the rate of exergy destroyed in the compressor is given by

$$I_{compressor} = T_0\dot{m}(s_4 - s_3). \quad (10)$$

For the condenser, the rate of exergy destroyed is expressed as

$$I_{condenser} = T_0\left[\dot{m}(s_7 - s_4) + \frac{Q_{condenser}}{T_{condenser}}\right] = T_0\dot{m}\left[(s_7 - s_4) + \frac{(h_4 - h_7)}{T_{condenser}}\right]. \quad (11)$$

With no heat transferred during the expansion process, the rate of exergy destroyed in the throttling valves is given by

$$I_{throttle} = T_0\dot{m}(s_1 - s_7). \quad (12)$$

The rate of exergy destroyed in each component is calculated for the mass velocity range of $G_{avionics}$ = 151.21–264.63 kg/m$^2$ s ($\dot{m} = 151.21 \times 10^{-4}$ – $264.63 \times 10^{-4}$ kg/s) and fixed heat flux of $q''_{avionics}$ = 24,218.8 W/m$^2$, with zero heat input to the crew HX. Fig. 5(b) shows variations of irreversibilities for individual components and the entire cycle with $G_{avionics}$. Irreversibility of the avionics HX decreases with decreasing difference between heat sink

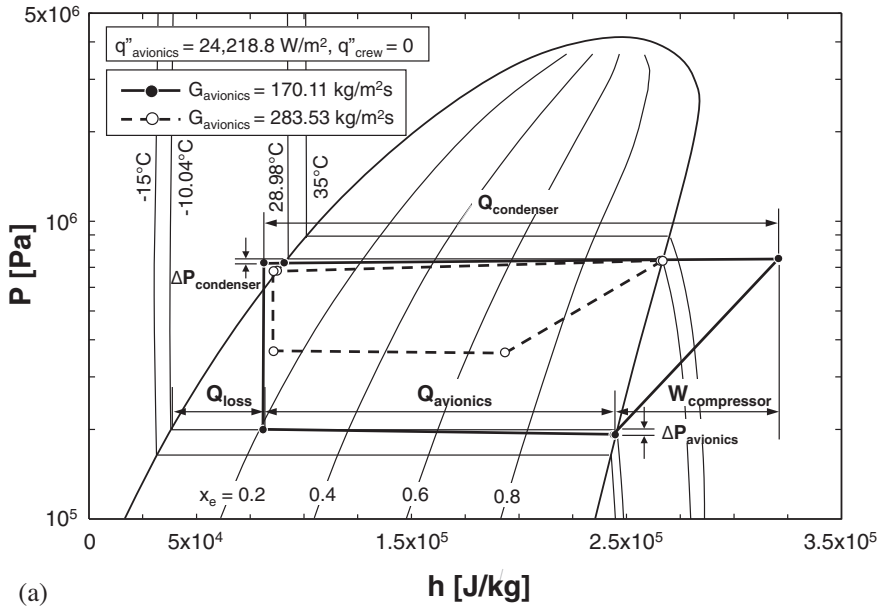


(a)

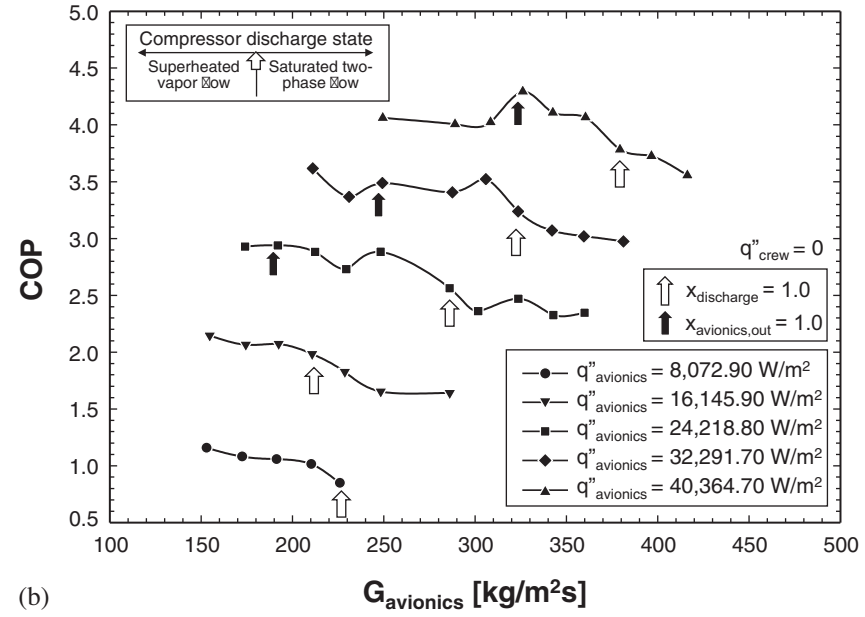


(b)

**Fig. 6.** (a) Pressure-enthalpy diagram for $G_{avionics}$ = 170.11 and 283.53 kg/m$^2$ s. (b) Variations of COP with mass velocity for different avionics HX heat loads.

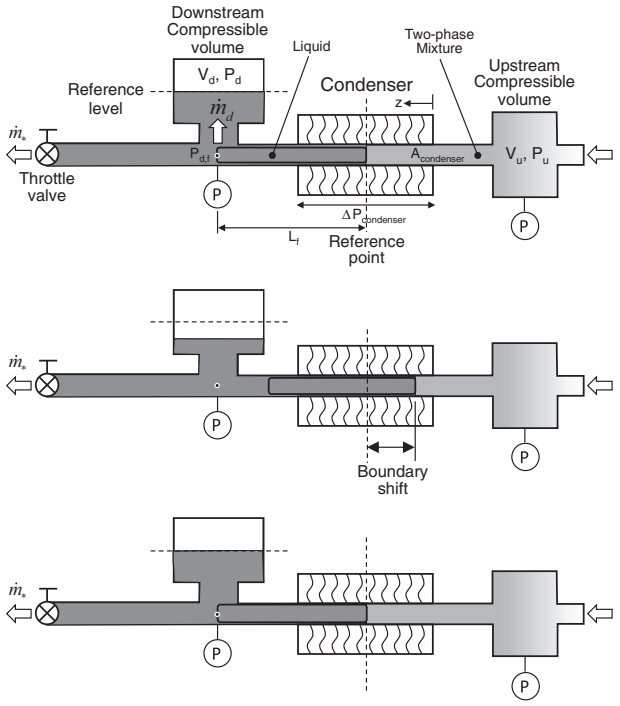


**Fig. 7.** Sequence of pressure oscillations at condenser inlet resulting from fluctuations in two-phase mixture/liquid interface, and pressure dampening by downstream liquid tank.

temperature, $T_{sink}$, and ambient temperature, $T_0 = 21.0\,^{\circ}C$. The highest avionics HX irreversibility values are encountered at the lowest $G_{avionics}$, corresponding to significant dryout, where $T_{sink}$ is highest, Fig. 3(b), and $h_{tp}$ lowest, Fig. 4(c). Fig. 5(b) shows increasing mass flow rate causes a monotonic increase in the compressor's irreversibility. With the condenser's saturation temperature of 28.68 °C slightly higher than the ambient temperature of 21.0 °C, the condenser's irreversibility is comparatively small. The irreversibility associated with the throttling process is similarly quite small. Adding all irreversibilities together yields the variation of $I_{total}$ with $G_{avionics}$ also depicted in Fig. 5(b), which shows a minimum at $G_{avionics} = 174.14\ kg/m^2\,s$ ($\dot{m} = 174.14 \times 10^{-4}\ kg/s$) corresponding to operating conditions yielding the smallest superheat at the avionics HX's outlet.

Fig. 6(a) compares pressure-enthalpy ($P$–$h$) diagrams for wet versus dry compression, corresponding to $G_{avionics} = 283.53$ and $170.11\ kg/m^2s$ ($\dot{m} = 283.53 \times 10^{-4}$ and $170.11 \times 10^{-4}\ kg/s$), respectively, for equal compressor discharge pressures. For dry compression corresponding to $G_{avionics} < 170.11\ kg/m^2s$, the refrigerant enters the compressor in superheated vapor state, and is superheated further at the compressor exit. Wet compression is achieved when $G_{avionics} > 170.11\ kg/m^2s$, which poses compressor reliability concerns.

The coefficient of performance ($COP$), defined as the ratio of heat input to work input,

$$COP = \frac{Q_{avionics}}{W_{compressor}} = \frac{h_{avionics,out} - h_{avionics,in}}{h_{compresor,out} - h_{avionics,out}}, \tag{13}$$

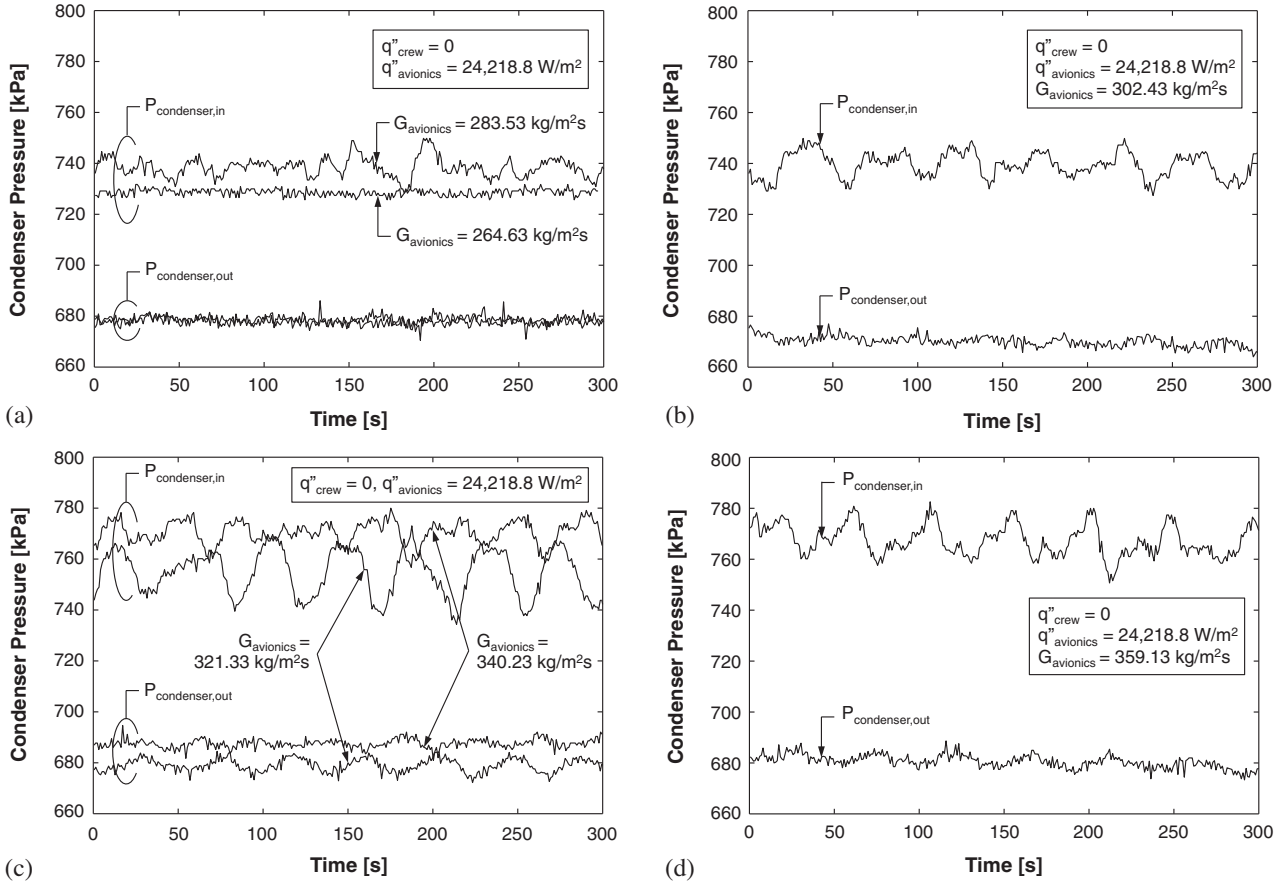


**Fig. 8.** Temporal records of condenser's inlet and outlet pressures at $q''_{avionics} = 24{,}218.8\ W/m^2$ for (a) $G_{avionics} = 264.63$ and $283.53\ kg/m^2\,s$, (b) $G_{avionics} = 302.43\ kg/m^2\,s$, (c) $G_{avionics} = 321.33$ and $340.23\ kg/m^2\,s$, and (d) $G_{avionics} = 359.13\ kg/m^2\,s$.

is a key measure of thermodynamic effectiveness. Fig. 6(b) shows variations of *COP* with $G_{avionics}$ for different values of $q''_{avionics}$, *i.e.*, different heat loads. In this plot, measured values of $Q_{avionics}$ and $W_{compressor}$ are used. *COP* is shown increasing with increasing heat input but decreases with increasing flow rate because of the increase in compressor work. The open arrows in Fig. 6(b) indicate where the compressor's discharge temperature is equal to the condenser's saturation temperature, *i.e.*, where the refrigerant exits the compressor as saturated vapor. These arrows mark the conditions where *COP* begins to decrease appreciably with increasing flow rate. This is where compressor work increases appreciably because of both increasing flow rate and increased liquid droplet inflow. This is also where the likelihood of mechanical failure of the scroll compressor increases. The open arrows therefore serve as useful guides for operational limits of the refrigeration cycle. The solid arrows in Fig. 6(b) correspond to avionics HX's outlet quality of unity. Flow rates smaller than those indicated by the solid arrows yield superheated vapor conditions at the compressor's inlet, which increase compressor work because of increased specific volume [34,42]. The solid arrow for $q''_{avionics}$ = 40,364.70 W/m$^2$ indicates the highest *COP* where compressor work is smallest because of the combination of small specific volume and moderate flow rate.

## 4. Condenser flow oscillations

### 4.1. Pressure oscillations in condenser

As discussed earlier, pressure oscillations associated with the chugging phenomenon have been explored analytically for a pipe supplying steam into a subcooled water pool [33]. During this direct condensation process, the steam-water interface was observed to oscillate along the pipe, resulting in periodic pressure oscillations in the steam pipe's header.

Notice in Fig. 1(a) the existence of an oil separator and liquid tank upstream and downstream of the condenser, respectively. Compressible volumes within each, along with liquid inertia within the condenser tubes, create the possibility of pressure oscillations at the condenser's inlet and outlet, loosely resembling those of the chugging phenomenon just described.

As shown in the top schematic in Fig. 7, the volume upstream of the condenser, which accounts for the oil separator, is modeled as upstream plenum with compressible volume $V_u$ and pressure $P_u$. Downstream from the condenser, another volume, associated with the liquid tank, is modeled as downstream plenum with compressible volume $V_d$ and pressure $P_d$. The interface between upstream two-phase mixture and downstream liquid in the condenser tubes where $x_{e,condenser} = 0$ is assumed to fluctuate. This dynamic system is dictated by interactions between the upstream and downstream compressible volumes, and inertia of liquid section of length $L_f$ extending from this interface to the inlet of the liquid tank, ignoring the contribution of the comparatively weak inertia of the upstream two-phase mixture. As shown in the second schematic in Fig. 7, a decrease in upstream pressure $P_u$ moves the interface within the condenser tube upstream, causing liquid level in the liquid tank to drop in order to maintain a fairly constant mass flow rate, $\dot{m}_*$, at the throttling valves. This interface shift now causes a decrease in $V_u$ and increase in $P_u$. As shown in the third schematic in Fig. 7, the now increased $P_u$ pushes the liquid section down-

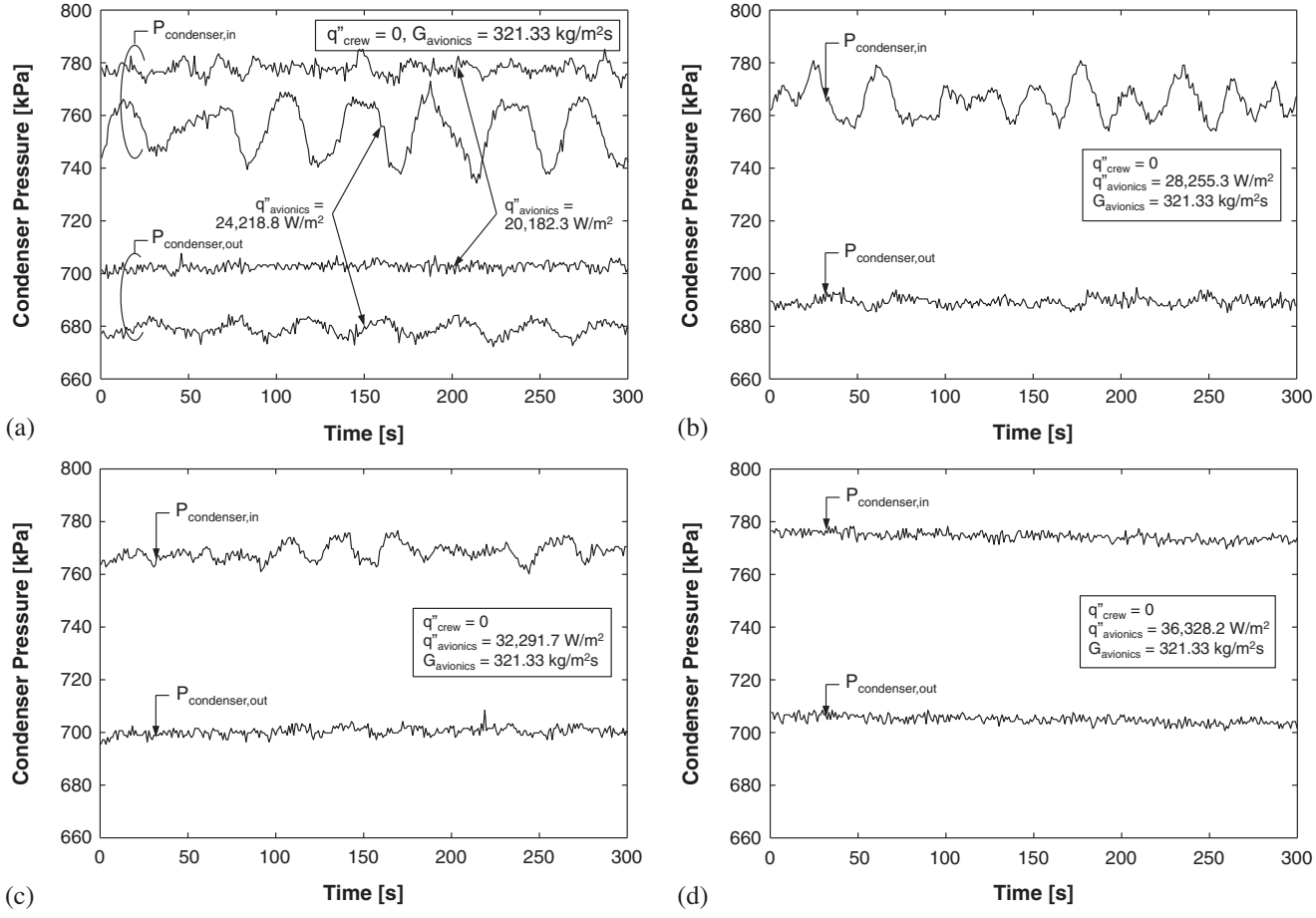


**Fig. 9.** Temporal records of condenser's inlet and outlet pressures at $G_{avionics}$ = 321.33 kg/m$^2$s for (a) $q''_{avionics}$ = 20,182.3 and 24,218.8 W/m$^2$, (b) $q''_{avionics}$ = 28,255.3 W/m$^2$, (c) $q''_{avionics}$ = 32,291.7 W/m$^2$, and (d) $q''_{avionics}$ = 36,328.2 W/m$^2$.

stream, raising liquid level in the liquid tank to the initial reference level to maintain the same flow rate at the throttling valves. This completes an oscillation cycle, which is repeated in a periodic manner.

### 4.2. Pressure oscillation results

Increasing the refrigerant's mass flow rate for fixed heat input decreases both the crew HX's inlet quality (because of reduced throttling) and quality change across the crew HX. Similarly, an increase in mass flow rate decreases both the avionics HX's inlet quality and quality change across the avionics HX; the decreased quality change can be explained by the relation

$$x_{e,avionics,out} = x_{e,avionics,in} + \frac{q''_{avionics} A_{base,avionics}}{\dot{m}_{avionics} h_{fg}}. \quad (14)$$

Therefore, the amount of liquid in the liquid tank decreases with increasing mass flow rate as pressure difference across the throttling valves decreases and liquid moves to the evaporator side of the loop.

The amount of liquid in the liquid tank influences stiffness of the condenser system illustrated in Fig. 7, defined as

$$stiffness = \left(\frac{dP_d}{dV_d}\right)_0 \quad (15)$$

where '0' represents the reference liquid level indicated in the top schematic in Fig. 7. Decreased stiffness triggers stronger variations in mass flow, $\dot{m}_d$, to the liquid tank.

Fig. 8(a)–(d) show temporal records of the condenser's inlet and outlet pressure for $q''_{avionics}$ = 24,218.8 W/m$^2$ and different flow rates. Notice that pressure oscillations are far more significant upstream than downstream, which can be explained by the downstream liquid tank having larger volume and therefore smaller stiffness. Fig. 8(a) shows the condenser's inlet pressure oscillations are quite small for $G_{avionics}$ = 264.63 kg/m$^2$s but begin to grow in amplitude as $G_{avionics}$ is increased to 283.53 kg/m$^2$s. The amplitude continues to increase at $G_{avionics}$ = 302.43 kg/m$^2$s, Fig. 8(b), and reaches peak value at $G_{avionics}$ = 321.33 kg/m$^2$s, Fig. 8(c), above which it begins decreasing at $G_{avionics}$ = 340.23 kg/m$^2$s, Fig. 8(c), and $G_{avionics}$ = 359.13 kg/m$^2$s, Fig. 8(d).

Pressure oscillations are also influenced by heat input to the avionics HX, because the amount of liquid in the condenser and liquid tank increases with an increase in quality rise, $\Delta x_{e,avionics}$ ($= x_{e,avionics,out} - x_{e,avionics,in}$) across the avionics HX. The condenser's upstream and downstream pressure oscillations grow in amplitude as $q''_{avionics}$ is increased from 20,182.3 to 24,218.8 W/m$^2$, Fig. 9(a), then begin to decrease as $q''_{avionics}$ is increased to 28,255.3 W/m$^2$, Fig. 9(b). The upstream pressure oscillations continue to weaken as $q''_{avionics}$ is increased to 32,291.7 W/m$^2$, Fig. 9(c), before subsiding significantly at 36,328.2 W/m$^2$, Fig. 9(d).

To investigate the effects of mass flow rate and heat flux on pressure oscillations, the amplitude and period of the condenser's inlet pressure signal are examined separately as shown in Fig. 10 (a) and (b), respectively. The oscillation period $\tau$ in Fig. 10(b) is determined from the first terms in a Fourier series fit to the inlet pressure's temporal record,

$$P(t) = a_0 + a_1 \cos \omega t + b_1 \sin \omega t, \quad (16)$$

$$\text{where} \quad \tau = \frac{2\pi}{\omega} \quad (17)$$

and $\omega$ is the angular frequency in Hz. Also indicated in Fig. 10 (a) and (b) are resonance effects associated with the upstream plenum's compressible volume in Fig. 7. This volume is modeled as a Helmholtz resonator with a long oscillating liquid section, whose Helmholtz resonance frequency, $f$, is expressed as [43]

$$f = \frac{v}{2\pi}\sqrt{\frac{A_{pipe}}{V_u L_f}}, \quad (18)$$

where $v$ is the speed of sound of superheated vapor or two-phase flow in the upstream compressible volume. Eq. (18) shows frequency is inversely proportional to the product of compressible volume, $V_u$, and the length $L_f$ of the liquid section.

Fig. 10(a) shows peak oscillation amplitude is achieved at an intermediate value of $q''_{avionics}$ for each value of $G_{avionics}$, similar to the trend captured in Fig. 9(a)–(d). The oscillation is magnified most when compressible volume stiffness and liquid section inertia are tuned for resonance, which is why the pressure oscillation is highest in the intermediate ranges of mass flow rate and heat flux. Fig. 10(b) shows peak oscillation period is also achieved at an intermediate value of $q''_{avionics}$ for each value of $G_{avionics}$, and the period decreases as stiffness shifts away from the peak point.

### 4.3. Mass Flow Rate Oscillation Results

The condenser's pressure fluctuations also influence mass flow rate, which is related to pressure drop across the throttling valves, $\Delta P_{throttle} = P_{condenser,out} - P_{crew,in}$ according to

$$\dot{m}_0 = \gamma \Delta P_{throttle}, \quad (19)$$

where $\gamma$ is related to flow coefficient ($Cv$) and number of turns of the throttling valves. Fig. 11(a)–(c) show fluctuations in the mass flow rate are in phase with those of pressure drop across the throttling

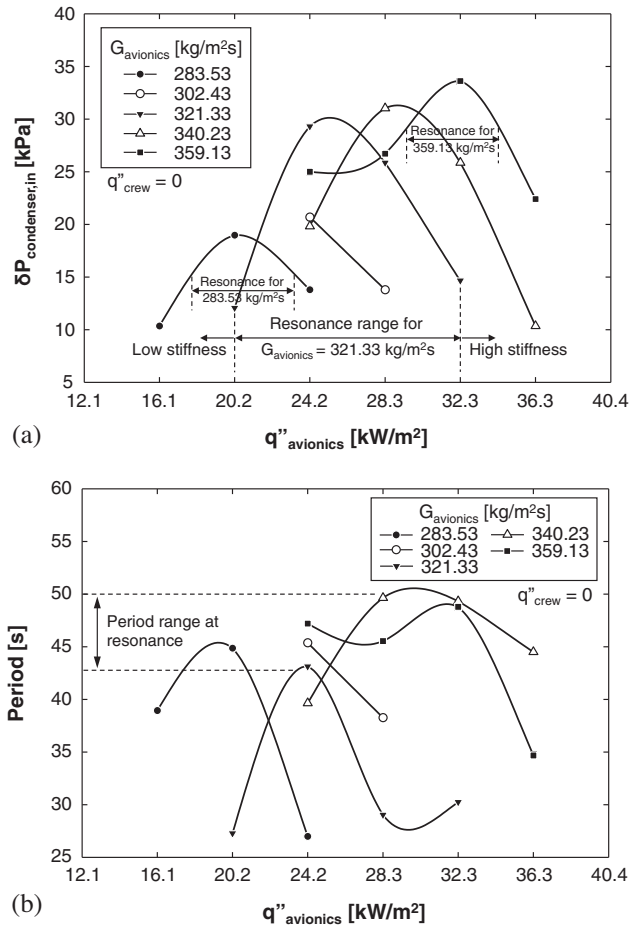


**Fig. 10.** Variations of (a) amplitude and (b) period of condenser's inlet pressure with avionics HX's heat flux for different values of $G_{avionics}$.

valves. The flow rate fluctuations acquire highest amplitude at $\overline{G}_{avionics}$ = 359.13 kg/m$^2$ s, while pressure drop oscillations are highest at $\overline{G}_{avionics}$ = 321.33 kg/m$^2$ s.

Figs. 12(a)–(c) show the impact of heat flux on the fluctuations in $\Delta P_{throttle}$ and $G_{avionics}$. They reveal the fluctuations in mass flow rate decrease with increasing $q''_{avionics}$, which indicates the resistance of the throttling valves needs to increase as the amount of liquid stored in the liquid tank increases.

## 5. Conclusion

This paper investigated the heat transfer characteristics of two large area micro-channel heat exchangers, crew HX and avionics HX, that are incorporated as evaporators in a refrigeration cycle, as well as the thermodynamic performance of the cycle. Particular attention was also given to system instability in the form of pressure and flow rate oscillations.

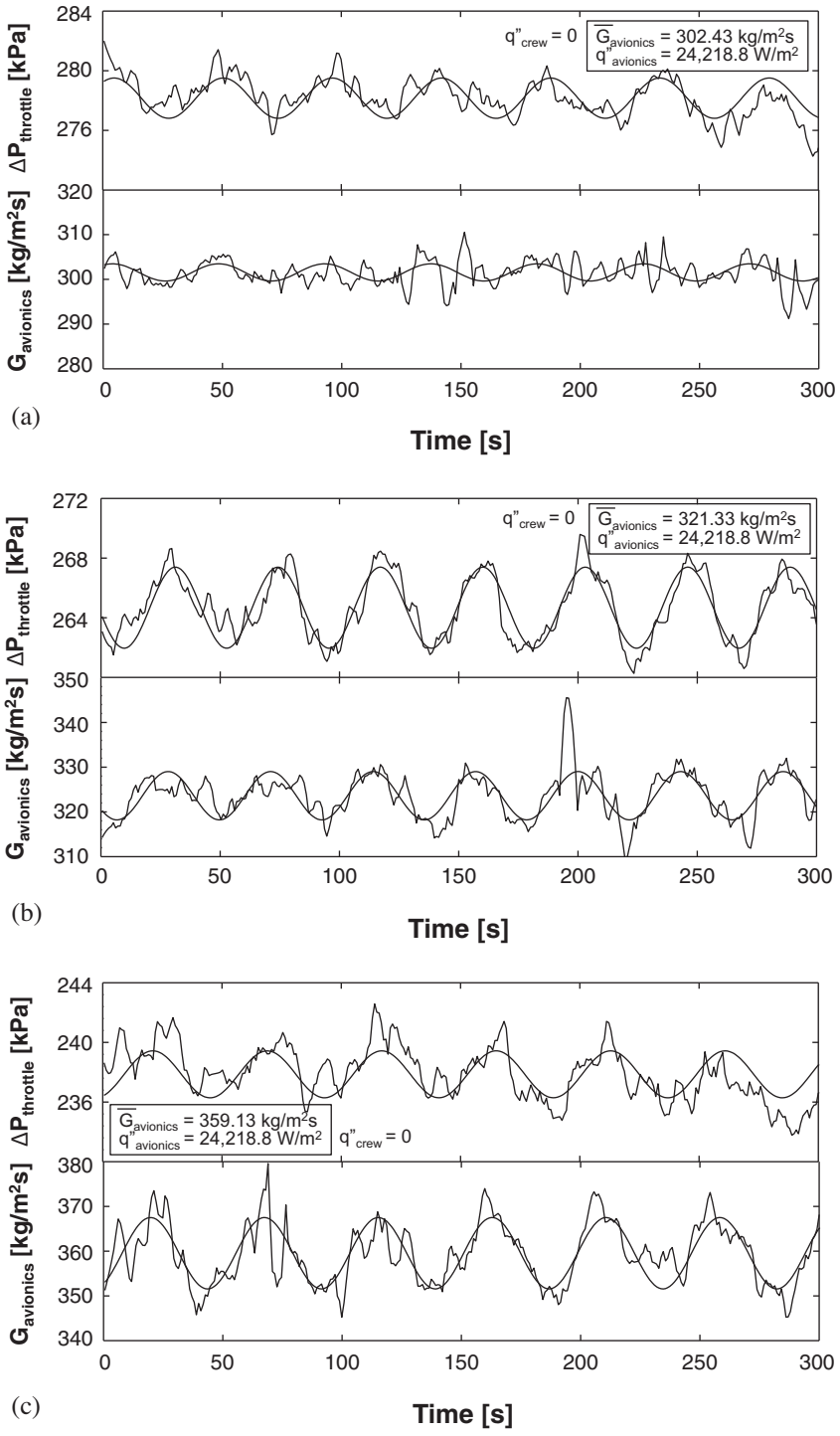


**Fig. 11.** Temporal records of pressure drop across throttling valves and avionics HX mass velocity at $q''_{avionics}$ = 24,218.8 W/m$^2$ for mean mass velocities of (a) 302.43 kg/m$^2$ s, (b) 321.33 kg/m$^2$ s, and (c) 359.13 kg/m$^2$ s.

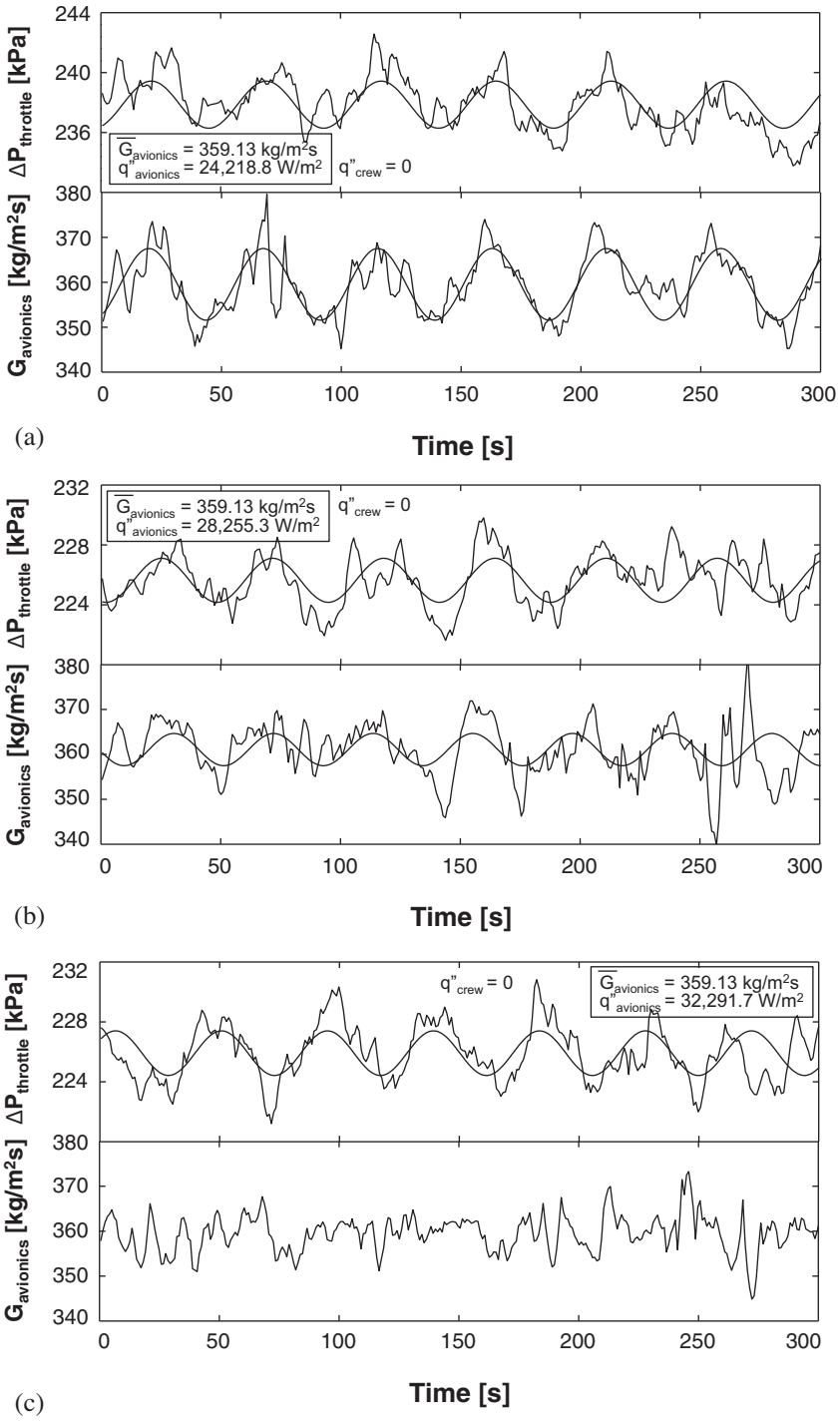


**Fig. 12.** Temporal records of pressure drop across throttling valves and avionics HX mass velocity at $G_{avionics}$ = 359.13 kg/m²s for (a) $q''_{avionics}$ = 24,218.8 W/m², (b) $q''_{avionics}$ = 28,255.3 W/m², and (c) $q''_{avionics}$ = 32,291.7 W/m².

(1) The heat transfer characteristics of the evaporators were investigated with the aid of axial distributions of both heat sink temperature and heat transfer coefficient. Different flow patterns and dryout effects are encountered in the evaporators. Relatively low quality values in the upstream crew HX are associated with bubbly/slug flow, with intermittent dryout in the liquid slug or liquid film surrounding elongated bubbles compromising heat transfer performance at low mass velocities. Higher qualities in the avionics HX are closely associated with annular flow, with dryout incipience in the annular film and eventual transition to mist flow at low mass velocities greatly reducing heat transfer performance in the downstream region of the evaporator.

(2) There is trade-off between optimum performances of the avionics HX and compressor, with former favoring outlet quality values below unity, corresponding to wet compression, to guard against downstream dryout, and the compressor favoring an avionics HX's outlet quality equal to or exceeding unity, corresponding to dry compression, to preclude internal damage to the compressor from entrained

droplets. Thermodynamic analysis of the refrigeration cycle shows exergy destruction is minimum when the avionics HX's outlet quality is close to unity.

(3) A combination of compressible volumes both upstream and downstream of the condenser, and inertia of liquid in the condenser renders the system susceptible to instabilities in the form of condenser inlet and outlet pressure oscillations for fixed mass flow rate. These pressure oscillations are sensitive to both flow rate and evaporator heat input. Oscillations in the mass flow rate are dictated by the flow characteristics of the throttling valves, and are in phase with oscillations in pressure drop across the valves.

## Acknowledgement

The authors are grateful for the support of the National Aeronautics and Space Administration (NASA) under grant NNX13AB01G.

## References

[1] I. Mudawar, Assessment of high-heat-flux thermal management schemes, IEEE Trans. CPMT Compon. Packag. Technol. 24 (2001) 122–141.
[2] I. Mudawar, Two-phase microchannel heat sinks: theory, applications, and limitations, J. Electron. Packag. – Trans. ASME 133 (2011) 041002.
[3] D.B. Tuckerman, R.F.W. Pease, High-performance heat sinking for VLSI, IEEE Electron Device Lett. 2 (1981) 126–129.
[4] T.C. Willingham, I. Mudawar, Forced-convection boiling and critical heat flux from a linear array of discrete heat sources, Int. J. Heat Mass Transfer 35 (1992) 2879–2890.
[5] T.N. Tran, M.C. Chyu, M.W. Wambsganss, D.M. France, Two-phase pressure drop of refrigerants during flow boiling in small channels: an experimental investigation and correlation development, Int. J. Multiphase Flow 26 (2000) 1739–1754.
[6] H.J. Lee, S.Y. Lee, Pressure drop correlations for two-phase flow within horizontal rectangular channels with small heights, Int. J. Multiphase Flow 27 (2001) 783–796.
[7] H.J. Lee, S.Y. Lee, Heat transfer correlation for boiling flows in small rectangular horizontal channels with low aspect ratios, Int. J. Multiphase Flow 27 (2001) 2043–2062.
[8] W. Yu, D.M. France, M.W. Wambsganss, J.R. Hull, Two-phase pressure drop, boiling heat transfer, and critical heat flux to water in a small-diameter horizontal tube, Int. J. Multiphase Flow 28 (2002) 927–941.
[9] W. Li, Z. Wu, A general correlation for adiabatic two-phase pressure drop in micro/mini-channels, Int. J. Heat Mass Transfer 53 (2010) 2732–2739.
[10] J. Wu, T. Koettig, Ch. Franke, D. Helmer, T. Eisel, F. Haug, J. Bremer, Investigation of heat transfer and pressure drop of $CO_2$ two-phase flow in a horizontal minichannel, Int. J. Heat Mass Transfer 54 (2011) 2154–2162.
[11] M.H. Maqbool, B. Palm, R. Khodabandeh, Flow boiling of ammonia in vertical small diameter tubes: two phase frictional pressure drop results and assessment of prediction methods, Int. J. Therm. Sci. 54 (2012) 1–12.
[12] S. Mukherjee, I. Mudawar, Smart pumpless loop for micro-channel electronic cooling using flat and enhanced surfaces, IEEE Trans. CPMT: Compon. Packag. Technol. 26 (2003) 99–109.
[13] D.C. Wadsworth, I. Mudawar, Enhancement of single-phase heat transfer and critical heat flux from an ultra-high-flux simulated microelectronic heat source to a rectangular impinging jet of dielectric liquid, J. Heat Transfer – Trans. ASME 114 (1992) 764–768.
[14] M.K. Sung, I. Mudawar, Experimental and numerical investigation of single-phase heat transfer using a hybrid jet impingement/micro-channel cooling scheme, Int. J. Heat Mass Transfer 49 (2006) 682–694.
[15] M.K. Sung, I. Mudawar, Single-phase and two-phase hybrid cooling scheme for high-heat-flux thermal management of defense electronics, J. Electron. Packag. – Trans. ASME 131 (2009) 021013.
[16] P.E. Jimenez, I. Mudawar, A multi-kilowatt immersion-cooled standard electronic clamshell module for future aircraft avionics, J. Electron. Packag. – Trans. ASME 116 (1994) 220–229.
[17] M.B. Bowers, I. Mudawar, High flux boiling in low flow rate, low pressure drop mini-channel and micro-channel heat sinks, Int. J. Heat Mass Transfer 37 (1994) 321–332.
[18] J. Lee, I. Mudawar, Two-phase flow in high-heat-flux micro-channel heat sink for refrigeration cooling applications: part I––pressure drop characteristics, Int. J. Heat Mass Transfer 48 (2005) 928–940.
[19] J. Lee, I. Mudawar, Two-phase flow in high-heat-flux micro-channel heat sink for refrigeration cooling applications: part II—heat transfer characteristics, Int. J. Heat Mass Transfer 48 (2005) 941–955.
[20] J. Lee, I. Mudawar, Implementation of microchannel evaporator for high-heat-flux refrigeration cooling applications, J. Electron. Packag. – Trans. ASME 128 (2005) 30–37.
[21] J.A. Boure, A.E. Bergles, L.S. Tong, Review of two-phase flow instability, Nucl. Eng. Des. 25 (1973) 165–192.
[22] S. Kakaç, B. Bon, A review of two-phase flow dynamic instabilities in tube boiling systems, Int. J. Heat Mass Transfer 51 (2008) 399–433.
[23] T. Doğan, S. Kakaç, T.N. Veziroğlu, Analysis of forced-convection boiling flow instabilities in a single-channel upflow system, Int. J. Heat Fluid Flow 4 (1983) 145–156.
[24] N. Zuber, J.A. Findlay, Average volumetric concentration in two-phase flow systems, J. Heat Transfer – Trans. ASME 87 (1965) 453–468.
[25] A.H. Stenning, T.N. Veziroğlu, Flow oscillation modes in forced-convection boiling, Proc. 1965 Heat Transfer Fluid Mechanics Institute, Stanford University Press, pp. 301–316.
[26] A.H. Stenning, T.N. Veziroğlu, G.M. Callahan, Pressure-drop oscillations in forced convection flow with boiling, EURATOM Symp. Two-Phase Flow Dynamics, Eindhoven, Netherlands, 1967, pp. 405–427.
[27] J.S. Maulbetsch, P. Griffith, A study of system-induced instabilities in forced-convection flows with subcooled boiling Tech. Report No. 5382-35, Dept. of Mechanical Engineering, Massachusetts Institute of Technology, Cambridge, MA, 1965.
[28] M. Ozawa, S. Nakanishi, S. Ishigai, Y. Mizuta, H. Tarui, Flow instabilities in boiling channels: part 1 pressure drop oscillation, Bull. JSME 22 (1979) 1113–1118.
[29] E.M. Greitzer, The stability of pumping systems – the 1980 Freeman scholar lecture, J. Fluids Eng. 103 (1981) (1980) 193–242.
[30] W. Qu, I. Mudawar, Measurement and prediction of pressure drop in two-phase micro-channel heat sinks, Int. J. Heat Mass Transfer 46 (2003) 2737–2753.
[31] W. Qu, I. Mudawar, Transport phenomena in two-phase micro-channel heat sinks, J. Electron. Packag. – Trans. ASME 126 (2004) 213–224.
[32] M.-H. Chun, Y.-S. Kim, J.-W. Park, An investigation of direct condensation of steam jet in subcooled water, Int. Commun. Heat Mass Transfer 23 (1996) 947–958.
[33] H. Nariai, I. Aya, Fluid and pressure oscillations occurring at direct contact condensation of steam flow with cold water, Nucl. Eng. Des. 95 (1986) 35–45.
[34] S.H. Lee, I. Mudawar, M.M. Hasan, Thermal analysis of hybrid single-phase, two-phase and heat pump thermal control system (TCS) for future spacecraft, Appl. Therm. Eng. 100 (2016) 190–214.
[35] S. Lee, I. Mudawar, Investigation of flow boiling in large micro-channel heat exchangers in a refrigeration loop for space applications, Int. J. Heat Mass Transfer 97 (2016) 110–129.
[36] S. Lee, I. Mudawar, Transient characteristics of flow boiling in large micro-channel heat exchangers, Int. J. Heat Mass Transfer 103 (2016) 186–202.
[37] T.L. Bergman, F.P. Incropera, A.S. Lavine, D.P. DeWitt, Fundamentals of Heat and Mass Transfer, seventh ed., Wiley and Sons, New York, 2011.
[38] R. Yumrutaş, M. Kunduz, M. Kanoğlu, Exergy analysis of vapor compression refrigeration systems, Exergy Int. J. 2 (2002) 266–272.
[39] E. Bilgen, H. Takahashi, Exergy analysis and experimental study of heat pump systems, Exergy Int. J. 2 (2002) 259–265.
[40] J.U. Ahamed, R. Saidur, H.H. Masjuki, A review on exergy analysis of vapor compression refrigeration system, Renewable Sustainable Energy Rev. 15 (2011) 1593–1600.
[41] A. Bejan, Entropy generation minimization: the new thermodynamics of finite-size devices and finite-time processes, J. Appl. Phys. 79 (1996) 1191–1218.
[42] P.A. Domanski, D.A. Didion, J.P. Doyle, Evaluation of suction-line/liquid-line heat exchange in the refrigeration cycle, Int. J. Refrig. 17 (1994) 487–493.
[43] H. Helmholtz, Theorie der Lluftschwingungen in röhren mit offenen enden, J. Reine Angew. Math. 57 (1860) 1–72.